A dynamic flotation model to infer process characteristics from online measurements

D. J. Oosthuizen[a,b], J. D. le Roux[b], I. K. Craig[b,*]

[a] *Process IQ, Perth, Australia.*
[b] *Department of Electrical, Electronic and Computer Engineering, University of Pretoria, Pretoria, South Africa.*

Abstract

A dynamic flotation model incorporating fundamental and phenomenological relationships, information from froth images and steady-state models is described. Model outputs correspond with online measurements commonly available on flotation circuits, and the model parameters are estimated from industrial data. Simulation results are presented, highlighting important non-linearities that need to be taken into account for optimal flotation operation. Observability and controllability analyses are performed, proving that key flotation parameters can theoretically be estimated from online process measurements, and that the set of modelled inputs can control all the model outputs. This model can be used in advanced model-based control and optimisation applications. The ability to estimate key flotation parameters opens up opportunities for improved optimisation of operating variables such as aeration rates, froth depth and the reagent recipe.

Keywords: flotation, modelling, process control, simulation, optimisation

1. Introduction

Model based flotation control has been used in industry for over 25 years (Schubert et al., 1995). The first applications focussed mostly upon stabilising pulp levels (Jämsä-Jounela et al., 2003) - an aspect that remains relevant and is still improved on (Shean et al., 2018). Flotation stabilisation furthermore continues to add considerable economic benefit as part of advanced control implementations (Saffy et al., 2019).

Stabilisation of flotation cells originated from the need to stabilise the flotation process before optimisation can be attempted. The role of the froth phase and water transport mechanism in flotation grade and recovery optimisation was modelled by Bascur and Herbst (1982), using a combination of fundamental, phenomenological and empirical models. Neethling and Cilliers (2003) contributed significantly to understanding the mechanisms in the froth phase through fundamental and phenomenological models, as well as simplified versions of these models (Neethling and Cilliers, 2009), while Hadler and Cilliers (2009) focussed on the application of these models in maximising grade and recovery. Image analysis has also been used extensively in quantifying flotation behaviour (Aldrich et al., 2010).

Regardless of whether empirical, fundamental or phenomenological models are used - the number and nature of parameters used in these models often require sampling and modelling campaigns that are much more extensive (and potentially disruptive) than routine sampling commonly conducted on flotation processes. As a result, some model parameters will not be updated regularly, resulting in a gradual deterioration in model accuracy. The ability of a model to estimate the key flotation parameters from online measurements not only lessens the reliance of the model on periodic manual updates, but also ensures that parameters track short-term variations in process characteristics that occur between manual samples.

In this work existing models available in literature are combined into a model structure that allows the estimation of model parameters from online process measurements. Sections 2.1 and 2.2 show fundamental

*Corresponding author. Address: Department of Electrical, Electronic, and Computer Engineering, University of Pretoria, Pretoria, South Africa. Tel.: +27 12 420 2172; Fax: +27 12 362 5000. E-mail: ian.craig@up.ac.za

mass- and volume balance models as the core of the model. The concentrate volumetric flow rate is described in Section 2.3 and is based on steady-state models (Neethling and Cilliers, 2009). Section 2.4 describes the concentrate mass flow model, combining a dynamic kinetic model for true flotation (Polat and Chander, 2000) with a steady-state model for entrainment. A simplification of the entrainment model is also shown. Section 2.5 describes bubble size and air recovery models, and the derivation of linear relationships to model bubble size and air recovery based on data collected on an industrial plant (Hadler et al., 2010). A steady-state simulation of the model is shown in Section 3, using operating ranges from an industrial plant as described by Hadler et al. (2010). An observability and controllability analysis is done in Section 4, showing that in theory the model parameters can be estimated from online measurements, and that the process can be manipulated to achieve a desired operating point.

2. Model Description

2.1. Volume balance

Mass and volume balances govern the transfer of materials between cells and the concentrate and tailings streams. Fig. 1 is an example of the volumetric flow rates between three flotation cells and a concentrate hopper.

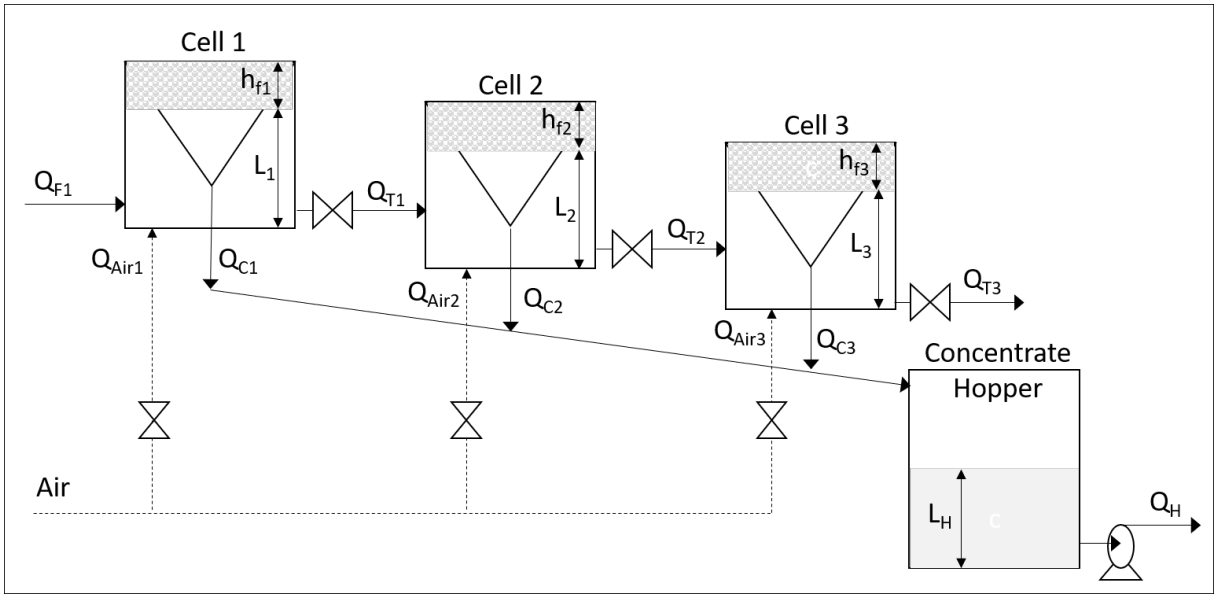

Figure 1: Volumetric flow rates between 3 flotation cells and a concentrate hopper

The volumetric feed flow rate and density are typically measured, and feed composition is either measured or, if not, known fairly accurately. For each cell k, the volume balance can be written, with Q_{F_k} the volumetric feed flow rate to cell k, Q_{T_k} the volumetric tailings flow rate from cell k, and Q_{C_k} the concentrate flow rate from cell k. The change in cell pulp volume, V_k, can be rewritten in terms of the cell surface area A_k, and pulp level L_k, assuming a uniform cell surface area over its typical operating range.

$$\frac{dV_k}{dt} = A_k \frac{dL_k}{dt} = Q_{F_k} - Q_{T_k} - Q_{C_k} \tag{1}$$

The tailings flow rate from cell k is the feed to cell $k+1$ ($Q_{T_k} = Q_{F_{k+1}}$). No attempt will be made to model tailings flow rate from cell levels and valve characteristics as was done by Jämsä-Jounela et al. (2003), as valves in industrial environments often have considerable hysteresis, and flow rate through a valve

is influenced by a variety of process disturbances such as density. Instead, Q_{C_k} will be calculated from the water recovery calculation described by Neethling and Cilliers (2009), and it is assumed that a controller exists to control Q_{T_k} to a desired flow rate.

For the concentrate hopper with level L_H, and surface area A_H, the volume balance includes the concentrate inflows from all N contributing cells ($Q_{C_1} + Q_{C_2} + ... + Q_{C_N}$), and the outflow from the hopper (Q_H).

$$\frac{dV_H}{dt} = A_H \frac{dL_H}{dt} = Q_{C_1} + Q_{C_2} + ... + Q_{C_n} - Q_H \tag{2}$$

2.2. Mass balance

The mass flow rates between cells are modelled using a mass balance, with the feed mass flow rate $\dot{M}^{i,j}_{F_k}$, into cell k calculated from the feed volume, density and composition. The mass flow rates of different mineral species i, are modelled separately to distinguish between desired (usually floatable) minerals containing the elements that the flotation circuit aims to recover, and other gangue or undesired minerals. In addition, each species can be divided into multiple classes j, where each class could have different floatability characteristics (Oosthuizen and Craig, 2018) and/or different size distributions affecting entrainment. The symbols are described in Table 1.

Table 1: Mass balance symbols

Variable	Unit	Description
i	-	Superscript for mineral species (e.g. gangue or valuable mineral)
j	-	Superscript for mineral class with different floatability or size
k, H	-	Subscript for unit (flotation cell k, or hopper, H)
$M^{i,j}_k$	kg	Accumulated mass of species i and class j, in cell k
Δ	-	Subscript for concentrate C, tailings T, and feed F
$\dot{M}^{i,j}_{\Delta_k}$	kg/h	Mass flow rate associated with a specific cell, k
Q_{Δ_k}	m^3/h	Volumetric flow rate associated with a specific cell, k

$$\frac{d}{dt} M^{i,j}_k = \dot{M}^{i,j}_{F_k} - \dot{M}^{i,j}_{T_k} - \dot{M}^{i,j}_{C_k} \tag{3}$$

For the flotation cells, the tailings mass flow rate from cell k equals the feed flow rate to cell $k+1$ ($\dot{M}^{i,j}_{F_{k+1}} = \dot{M}^{i,j}_{T_k}$). The tailings mass flow rates from each cell can be calculated as the tailings volumetric flow rate multiplied by the concentration of each species inside the flotation cell.

$$\dot{M}^{i,j}_{T_k} = \frac{M^{i,j}_k}{L_k A_k} Q_{T_k} \tag{4}$$

For the hopper, a similar approach can be followed, with the total hopper inflow being the sum of the concentrate flow rates from N contributing cells. The mass outflow rate ($\dot{M}^{i,j}_H$) is calculated as a function of the hopper concentrations and volumetric outflow rate. The hopper mass pull rate is then given by $\dot{M}^{Tot}_H$, for m and n the number of modelled mineral species and classes respectively.

$$\frac{d}{dt} M^{i,j}_H = \sum_{k=1}^{N} \dot{M}^{i,j}_{C_k} - \frac{M^{i,j}_H}{L_H A_H} Q_H \tag{5}$$

$$\dot{M}^{Tot}_H = \sum_{i=0}^{m} \sum_{j=0}^{n} \frac{M^{i,j}_H}{L_H A_H} Q_H \tag{6}$$

2.3. Concentrate volumetric flow rate

The concentrate volumetric flow rate from each cell, Q_{C_k}, can be calculated from the steady-state water recovery model given by Neethling and Cilliers (2009). For a two-phase system, Neethling and Cilliers (2003) showed that froth depth or froth residence time is not the main cause of reduced water recovery observed when the froth height increases (Wang et al., 2016; Zheng et al., 2006), but rather the increase in bubble size associated with deep froths. Neethling and Cilliers (2003) showed that water recovery has an inverse squared relation to bubble-diameter, with the proportionality constant determined by the bubble shape. The model for water recovery is shown in (7), where J_{gk} is the superficial gas velocity for cell k, and α_k is the air recovery for cell k. Eq. (8) defines the Plateau border length (λ_{out}) per volume of froth where D_{BF_k} is the mean top of froth bubble diameter for cell k. It is assumed for (8) that the bubbles have similar geometry as Kelvin cells (Neethling and Cilliers, 2003). k_1 defined in (9) quantifies the opposing forces acting on a particle due to gravity and viscosity, with ρ the fluid density, C_{PB} the Plateau border drag coefficient, and μ the fluid viscosity. J_{gk} as defined in (10) is calculated from the aeration rate Q_{air_k} of the flotation cell and its surface area A_k. Table 2 summarizes the variables for the water recovery model and provides the units for each variable.

Table 2: Variables used in concentrate flow rate and entrainment models (Neethling and Cilliers, 2009)

Variable	Description	Typical value	Units
J_{g_k}	Superficial gas velocity for cell k	10	mm/s
Q_{air_k}	Volumetric air flow rate to cell k	360	m^3/h
h_{f_k}	Froth depth	110	mm
α_k	Air recovery for cell k	0.25	$-$
D_{BF_k}	Mean top of froth bubble diameter for cell k	10	mm
$\rho_s^{i,j}$	Solid particle density for species i and class j	3000	kg/m^3
ρ	Fluid density	1000	kg/m^3
μ	Fluid viscosity	0.001	$Pa \cdot s$
g	Gravitational acceleration	9.81	m/s^2
d_{pmin}	Particle minimum diameter	10	μm
d_{pmax}	Particle maximum diameter	150	μm
C_{PB}	Plateau border drag coefficient	50	$-$
P_e	Dispersion Peclet number	0.15	$-$

$$\frac{Q_{C_k}}{A_k} = \begin{cases} \dfrac{{J_{g_k}}^2 \lambda_{out}}{k_1} (1-\alpha_k)\,\alpha_k & 0 < \alpha_k < 0.5 \\ \dfrac{{J_{g_k}}^2 \lambda_{out}}{4k_1} & \alpha_k \geq 0.5 \end{cases} \tag{7}$$

$$\lambda_{out} \approx \frac{6.81}{{D_{BF_k}}^2} \tag{8}$$

$$k_1 = \frac{\rho g}{3\,\mu\, C_{PB}} \tag{9}$$

$$J_{g_k} = 100 \frac{Q_{air_k}}{A_k} \tag{10}$$

2.4. Concentrate mass flow rate

The two main flotation mechanisms governing the transfer of material between the pulp and overflowing froth phases, are the true flotation of hydrophobic particles, and entrainment of all particles together with the bubble stream (Wills and Napier-Munn, 2006). True flotation is often modelled as a first order process,

while entrainment is a function of particle size, density and the upward stream of liquid (water recovery) as part of the bubble stream. The bulk of the desired mineral in the concentrate stream would typically be hydrophobic particles (due to true flotation), and the bulk of the gangue minerals in the concentrate stream, entrained particles. Both desired and gangue minerals are however entrained into the froth layer, and depressants are often required as a reagent to suppress weakly floatable gangue minerals. In this work, both true flotation and entrainment are modelled for all mineral species, to quantify the contribution of each mechanism to the final concentrate stream, and to provide insight into the effectiveness of the flotation reagents (depressants and activators). A model-based control system can optimise the true flotation and entrainment mass flows from each flotation cell, by exploiting differences in mineral species' concentrations among flotation cells and their impact on the combined concentrate streams grade and recovery.

2.4.1. True flotation model

True flotation is usually modelled using a kinetic model, based on a chemical reactor analogy, as described by Polat and Chander (2000) for a batch reactor. Such a model has the general form:

$$\frac{dC_{p_k}^{i,j}}{dt} = -K^{i,j}\, C_{p_k}^{i,j}\, C_{b_k}\, R_{f_k} \tag{11}$$

where $C_{p_k}^{i,j}$ represent the concentrations of particles of species i, class j in the pulp of cell k, and C_{b_k} represents the concentration of bubbles in the pulp. $K^{i,j}$ is a pseudo rate-constant that depends on various parameters affecting the flotation process. $K^{i,j}$ is modelled as a distribution with different values for each species i, and class j. R_{f_k} represents the froth recovery.

In this work the true flotation model of (11) is modified by setting R_{f_k} equal to the air recovery (α_k), described in Section 2.3. As the attachment of particles only takes place on the surfaces of bubbles, the effect of bubble surface area flux is taken into account by replacing C_{b_k} in (11) with a bubble surface area flux term (S_{b_k}) in (12), as described by Runge and Franzidis (2003). The change in concentration in the cell due to true flotation ($C_{p_k}^{i,j}$) is also replaced in (12) by a change in mass of each species and class ($M_k^{i,j}$) in flotation cell k. S_{b_k} is defined in (13), where D_{BP_k} is the Sauter mean bubble diameter in the pulp for cell k. Table 3 summarizes the variables for the true-flotation model and provides the units for each variable.

$$\frac{dM_k^{i,j}}{dt} = -K^{i,j}\, M_k^{i,j}\, S_{b_k}\, \alpha_k \tag{12}$$

$$S_{b_k} = 6\frac{J_{g_k}}{D_{BP_k}} \tag{13}$$

Table 3: Variables used in the true flotation model

Variable	Description	Units
D_{BP_k}	Sauter mean bubble diameter in pulp for cell k	mm
$C_{p_k}^{i,j}$	Concentrations of particles of species i, class j in the pulp of cell k	kg/m^3
$K^{i,j}$	Flotation rate-constant for species i, class j	$-$
R_{f_k}	Froth recovery for cell k, assumed to be equal to α_k	$-$
S_{b_k}	Bubble surface area flux for cell k	s^{-1}

2.4.2. Entrainment model

The entrainment model is based on the steady-state model by Neethling and Cilliers (2009), but is simplified to lump the effect of different size classes together. The original entrainment model of Neethling and Cilliers (2009) calculates an entrainment factor, $Ent^{i,j}$, to define the fraction of particles with a defined size, d_p, and density, $\rho_s^{i,j}$, that will be entrained for a specified J_{g_k} and froth depth, h_{f_k} (14). The variables and units for the entrainment model are defined in Table 2.

$$Ent^{i,j} \approx \begin{cases} exp\left(-\frac{{v_{set}^{i,j}}^{1.5} h_{f_k}}{D_{Axial}\sqrt{J_{g_k}\alpha_k(1-\alpha_k)}}\right) & 0 < \alpha_k < 0.5 \\ exp\left(-\frac{2{v_{set}^{i,j}}^{1.5} h_{f_k}}{D_{Axial}\sqrt{J_{g_k}}}\right) & \alpha_k \geq 0.5 \end{cases} \tag{14}$$

The particle settling velocity $v_{set}^{i,j}$, is described in (15), for species i and class j. The axial dispersion coefficient, D_{Axial}, is given by (16), where P_e is the dispersion Peclet number (Neethling and Cilliers, 2009).

$$v_{set}^{i,j} \approx \frac{1}{3}\frac{g\left(\rho_s^{i,j} - \rho\right) d_p^2}{18\mu} \tag{15}$$

$$D_{Axial} \approx \frac{J_{g_k}^{1.5}}{\sqrt{k_1\left(\sqrt{3} - \pi/2\right) P_e}} \tag{16}$$

$Ent^{i,j}$ is the ratio of the entrained solids concentration, $C_{c_k}^{i,j}$, to the slurry solids concentration, $C_{p_k}^{i,j}$.

$$Ent^{i,j} \approx \frac{C_{c_k}^{i,j}}{C_{p_k}^{i,j}} \tag{17}$$

Neethling and Cilliers (2009) noted that, although $Ent^{i,j}$ does not include a term for the froth bubble size, the water recovery defined in (7) is dependent on D_{BF_k}, implying that the entrained mass is a function of froth depth and froth bubble size.

Eq. (14) has a sharp transition between an entrainment factor of 0 and 1 over a narrow range in J_{g_k}, for a particular particle size, d_p. Using a single entrainment factor with an average particle size does not provide an accurate model with a gradual increase in entrainment (of particles of different sizes) as J_{g_k} increases, and using multiple entrainment factors to model different particle sizes quickly increases model dimensions beyond practical limits. A simplified entrainment factor $Ent_{var}^{i,j}$, based on the entrainment models described in (14 - 16) was consequently derived to describe entrainment of particles as a function of J_{g_k}, as given in (18). The main variables that will be manipulated are J_{g_k} and h_{f_k}. Therefore (14) can be rewritten as

$$Ent_{var}^{i,j} = exp(-\frac{K_{ent}^{i,j}\, h_{f_k}\, {d_{ptr}^{i,j}}^3}{{J_{g_k}}^2}) \tag{18}$$

where all other variables are lumped together in the single constant $K_{ent}^{i,j}$, defined as

$$K_{ent}^{i,j} = \left[\frac{1}{3}\frac{g\left(\rho_s^{i,j} - \rho\right)}{18\mu}\right]^{1.5} \frac{\sqrt{k_1\left(\sqrt{3} - \pi/2\right) P_e}}{\sqrt{\alpha_k(1-\alpha_k)}} \tag{19}$$

The particle diameter, $d_{ptr}^{i,j}$, for which the entrainment factor equals 0.5, can be calculated from (18) and (19) as

$$d_{ptr}^{i,j} = \sqrt[3]{\frac{\ln(0.5)\,{J_{g_k}}^2}{K_{ent}^{i,j}\, h_{f_k}}} \tag{20}$$

For smaller particles in particular, the entrainment factor changes from 0 to 1 over a fairly narrow range of superficial air velocities. Assuming that this transition occurs rapidly, and also assuming a flat size distribution profile over all size classes (on a log axis), the fraction of the material (of all size classes) entrained $Ent_{Frac}^{i,j}$, can be estimated as the ratio of the size class for which 50% is entrained over the total size range, where d_{pmin} and d_{pmax} represents the minimum and maximum ranges of the size classes modelled.

$$Ent^{i,j}_{Frac} = \frac{\ln(d^{i,j}_{ptr}) - \ln(d_{pmin})}{\ln(d_{pmax}) - \ln(d_{pmin})} \tag{21}$$

A comparison of the original entrainment factor $Ent^{i,j}$ in (14) (Neethling and Cilliers, 2009) and the simplified entrainment factor $Ent^{i,j}_{Frac}$ in (21) is shown in Fig. 2. This figure shows a good correlation over a wide range of J_{g_k}, between 0 and 1 cm/s. For the comparison shown in Fig. 2, $d_{pmin} = 8\mu m$, $d_{pmax} = 220\mu m$ and $\alpha_k = 0.5$ was used.

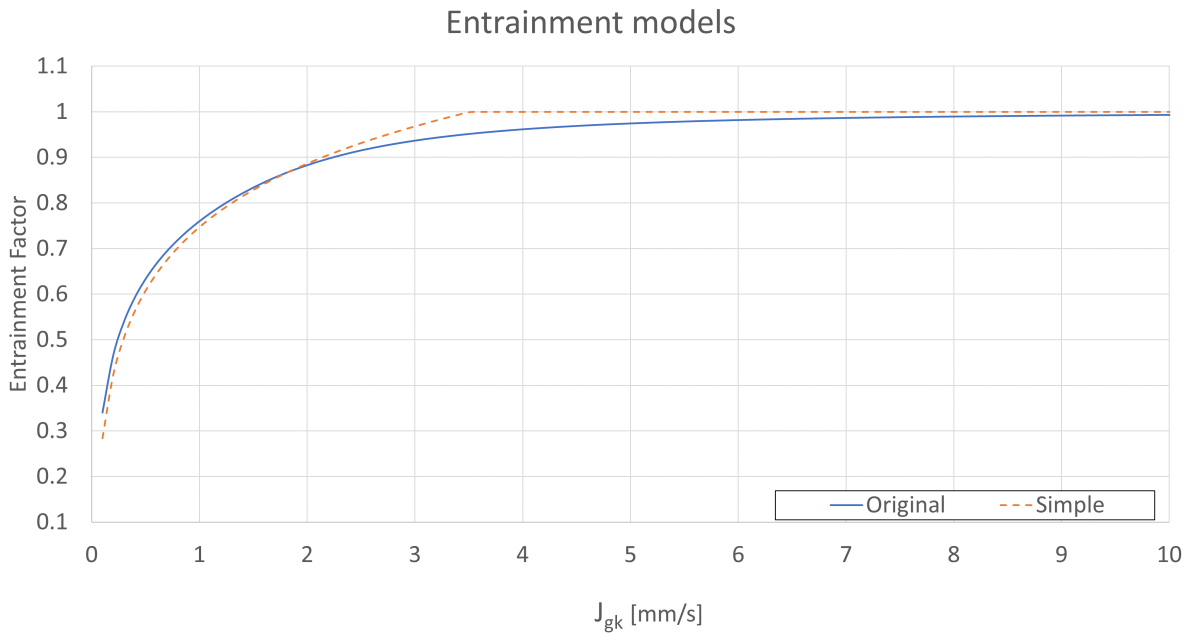

Figure 2: Comparison of original (14) and simplified (21) entrainment models

2.4.3. Combined concentrate flow rate

The overall concentrate mass flow rate from each cell $\dot{M}^{i,j}_{C_k}$, include true flotation and entrainment components. Combining (12), (17), (19) and (21) yields

$$\dot{M}^{i,j}_{C_k} = K^{i,j}\, M^{i,j}_k\, S_{b_k}\, \alpha_k + Ent^{i,j}_{Frac} \frac{M^{i,j}_k}{A_k\, L_k} Q_{C_k} \tag{22}$$

with $C^{i,j}_{p_k}$ in (17) defined in (23).

$$C^{i,j}_{p_k} = \frac{M^{i,j}_k}{A_k\, L_k} \tag{23}$$

The concentrate grade for each cell, $Grade_{C_k}$ can be calculated from (22) as the ratio of the desired element mass flow rate in the concentrate stream, $\dot{M}_{DC_k}$ (which may occur in a single or multiple mineral species) relative to the total concentrate mass flow rate. An "*instantaneous*" recovery, Rec_{C_k}, can be calculated as the ratio of the desired element mass flow rate in the concentrate stream relative to the desired element mass flow rate in the feed stream, $\dot{M}_{DF}$. Despite the "*instantaneous*" recovery not taking variability in the feed composition and residence times in the flotation circuit into account, it provides a useful real-time

approximation of recovery. The measured concentrate grade from the hopper, $Grade_H$ is calculated in (26) as the ratio between the desired mass, M_{D_H}, and the total masses in the concentrate hopper.

$$Grade_{C_k} = \frac{\dot{M}_{DC_k}}{\sum_{i=1}^{m}\sum_{j=1}^{n}\dot{M}_{C_k}^{i,j}} \tag{24}$$

$$Rec_{C_k} = \frac{\dot{M}_{DC_k}}{\dot{M}_{DF}} \tag{25}$$

$$Grade_H = \frac{M_{D_H}}{\sum_{i=1}^{m}\sum_{j=1}^{n}M_H^{i,j}} \tag{26}$$

2.5. Froth stability and bubble size models

The entrainment, water recovery and true flotation models described in (7), (12), (17) and (21) uses bubble size (D_{BF_k}) and froth recovery (α_k) as parameters. These are dynamic parameters that vary with operating conditions, and need to be modelled.

Several attempts have been made to model froth stability and the effect of the entrained and attached particles on froth stability − often with conflicting results (Ata, 2008; Tang and Tan, 1989). Zheng et al. (2006) and Barbian et al. (2003) reported a strong correlation between air recovery and the ratio between froth depth and $h_{froth-max}$, where $h_{froth-max}$ is an experimentally determined maximum depth that froth would grow to in a non-overflowing column. $h_{froth-max}$ is however not constant, but increases as a function of the aeration rate (Barbian et al., 2003). Although different measures of froth stability are used in literature, good correlations have been reported for some measures of bubble burst rates, dynamic froth stability, and air recovery (Morar et al., 2006).

The role of bubble size in froth stability was investigated by Geldenhuys and McFadzean (2019) and Gallegos-Acevedo et al. (2010). It was concluded that the top-of-froth bubble size in a non-overflowing column is determined by the bubble loading and is independent of the pulp bubble size. It was further shown that $h_{froth-max}$ follows a decaying trend with pulp bubble size. Ata (2008) performed experiments to determine the coalescence time of bubbles with varying surface coverings. It was shown that the relation between the coalescence time between two bubbles, and the percentage of their surface coverage is mostly linear. Gallegos-Acevedo et al. (2010) obtained similar results, but also showed how the average bubble size stabilised at a constant value of approximately 3mm for high bubble loadings, while the average bubble size exceeded 5 mm at lower loadings, indicating that further coalescence was inhibited at high bubble loadings.

Neethling and Cilliers (2003) included common probability functions to determine the probability that a bubble film would fail, in the models for both bubble coalescence and bubbles bursting at the top of the froth. Morar et al. (2012) used similar variables and fitted the bubble burst rate to a power function of both bubble size and bubble loading, but the sign of the power function was not consistent for all experiments. Despite agreement on the mechanisms affecting froth stability, Neethling and Brito-Parada (2018) concluded that the mechanisms for froth stability cannot be modelled with sufficient accuracy, and hence used an empirical relation to model froth stability and bubble size in combination with the fundamental water recovery model described in (7) - (9).

Empirical relationships were hence fitted to the measured top of froth bubble sizes D_{BF_k}, and air recoveries α_k, described in Hadler et al. (2010). D_{BF_k} was modelled as a linear combination of J_{g_k} and the froth residence time, λ_{air_k}, shown in (27), while α_k was modelled as a linear relation with J_{g_k} and D_{BF_k} shown in (28). $K_{BS_{Jg}}$, K_{BS_λ}, $K_{\alpha_{BF}}$ and $K_{\alpha_{Jg}}$ are the linear parameters that were calculated using data for 4 rougher cells. For D_{BF_k} an R^2 value of 0.84 was achieved for 4 rougher cells, while α_k had a much lower R^2 value of 0.55. Including bubble load in (28) resulted in an insignificant increase in accuracy, but it could be related to the dataset used.

$$\frac{d}{dt}D_{BF_k} = \frac{K_{BS_{Jg}}\,J_{g_k} + K_{BS_\lambda}\,\lambda_{air_k} - D_{BF_k}}{\lambda_{air_k}} \tag{27}$$

$$\frac{d}{dt}\alpha_k = \frac{K_{\alpha_{BF}}\, D_{BF_k} + K_{\alpha_{Jg}}\, J_{g_k} - \alpha_k}{\lambda_{air_k}} \tag{28}$$

$$\lambda_{air_k} = \frac{h_{f_k}}{J_{g_k}} \tag{29}$$

2.6. Model summary

The state equations for each flotation cell k, are summarised in Table 4, and the state equations for the concentrate hopper in Table 5. The "Online Measured" column in Tables 4 and 5 indicates if a state is measured. Additional measured model outputs (calculated from states) are shown in Table 6, measured disturbances in Table 7 and model parameters in Table 8.

Table 4: States for each Flotation Cell

Symbol	Eq.	State equation	Description	Online Measured
D_{BF_k}	(27)	$\frac{d}{dt}D_{BF_k} = \frac{K_{BS_{Jg}}\, J_{g_k} + K_{BS_\lambda}\, \lambda_{air_k} - D_{BF_k}}{\lambda_{air_k}}$	Top of froth bubble size	Yes
α_k	(28)	$\frac{d}{dt}\alpha_k = \frac{K_{\alpha_{BF}}\, D_{BF_k} + K_{\alpha_{Jg}}\, J_{g_k} - \alpha_k}{\lambda_{air_k}}$	Air recovery	Yes
L_k	(1)	$\frac{d}{dt}L_k = (Q_{F_k} - Q_{T_k} - Q_{C_k})/A_k$	Cell pulp level	Yes
$M_k^{i,j}$	(3)	$\frac{d}{dt}M_k^{i,j} = \dot{M}_{F_k}^{i,j} - \dot{M}_{T_k}^{i,j} - \dot{M}_{C_k}^{i,j}$	Masses in flotation cell	No

Table 5: States for the Concentrate Hopper

Symbol	Eq.	State equation	Description	Online Measured
L_H	(2)	$A_H \frac{dL_H}{dt} = Q_{C_1} + Q_{C_2} + ... + Q_{C_n} - Q_H$	Hopper level	Yes
$M_H^{i,j}$	(5)	$\frac{d}{dt}M_H^{i,j} = \sum_{k=1}^{N} \dot{M}_{C_k}^{i,j} - \frac{M_H^{i,j}}{L_H A_H} Q_H$	Masses in hopper	No

Table 6: Additional measured model outputs

Symbol	Eq.	Output equation	Description	Online Measured
$\dot{M}_H^{Tot}$	(6)	$\dot{M}_H^{Tot} = \sum_{i=0}^{m}\sum_{j=0}^{n} \frac{M_H^{i,j}}{L_H A_H} Q_H$	Mass pull rate	Yes
$Grade_H$	(26)	$Grade_H = \frac{M_{D_H}}{\sum_{i=1}^{m}\sum_{j=1}^{n} M_H^{i,j}}$	Concentrate grade in hopper	Yes

2.7. Interactions not modelled explicitly

The flotation model summarised in Section 2.6 does not explicitly model the effect of factors such as gas-holdup, pulp viscosity, turbulence, or reagents in the pulp on the recovery of different mineral species, as described by Bascur (2005). Instead, the effect of all factors contributing to the attachment and detachment of particles in the pulp are lumped together in a pseudo rate constant, $K^{i,j}$, as defined in (12). Where additional online measurements are available, more detailed sub-models can be developed to potentially improve model accuracy.

Table 7: Measured Disturbances

Symbol	Description	Unit
Q_{F_1}	Volumetric feed rate to cell 1	m^3/h
ρ_{F_1}	Feed density of slurry flow to cell 1	kg/m^3
$Grade_F^i$	Feed grade of species i to cell 1	-
d_{pmin}	Particle minimum diameter	μm
d_{pmax}	Particle maximum diameter	μm

Table 8: Model parameters to be estimated

Symbol	Description
$K_{BS_{J_g}}$	Effect of the superficial gas velocity on the mean top of froth bubble diameter
K_{BS_λ}	Effect of the average froth residence time on the mean top of froth bubble diameter
$K_{\alpha_{BF}}$	Effect of the mean top of froth bubble diameter on air recovery
$K_{\alpha_{J_g}}$	Effect of the superficial gas velocity on air recovery
C_{PB}	Plateau border drag coefficient
$K^{i,j}$	Flotation rate-constant for species i, class j

A key aspect of the model described in Section 2 is the ability to continuously estimate (and hence update) model parameters using online measurements. Future work to expand the model should ensure that all additional model parameters can also be estimated from online (or frequently updated) measurements, to prevent the expanded model from degrading over time.

3. Steady-state Model Simulation

Steady-state simulations were performed for a single flotation cell using the models described in Section 2, to show the dependence of the modelled variables on the controlled variables, J_{g_k} and h_{f_k}. Operating ranges and model outputs are based on the industrial data reported by Hadler et al. (2010). Simulation results of the empirical models of D_{BF_k} and α_k as described in (27) and (28) are shown in Fig. 3 and Fig. 4. Concentrate water recovery was simulated based on (7), including the dependence of D_{BF_k} and α_k on h_{f_k} and J_{g_k}. Grade and recovery simulations are based on true flotation (12) and the simplified entrainment model (21). The same ranges of J_{g_k} and h_{f_k} were used as what was described in Hadler et al. (2010), and model parameters were fitted to obtain similar results for these variables as was reported during this trial. Note that the experimental trial conducted by Hadler et al. (2010) focussed on the effect of J_{g_k} on α_k and other process variables, and that h_{f_k} was not varied intentionally as part of the test work.

Top of froth bubble size, D_{BF_k} (Fig. 3) and air recovery, α_k (Fig. 4) show peaks that occur at a lower value of J_{g_k} for shallower froths, as reported by Hadler et al. (2012). The values of J_{g_k} and h_{f_k} where the peaks occur are however different.

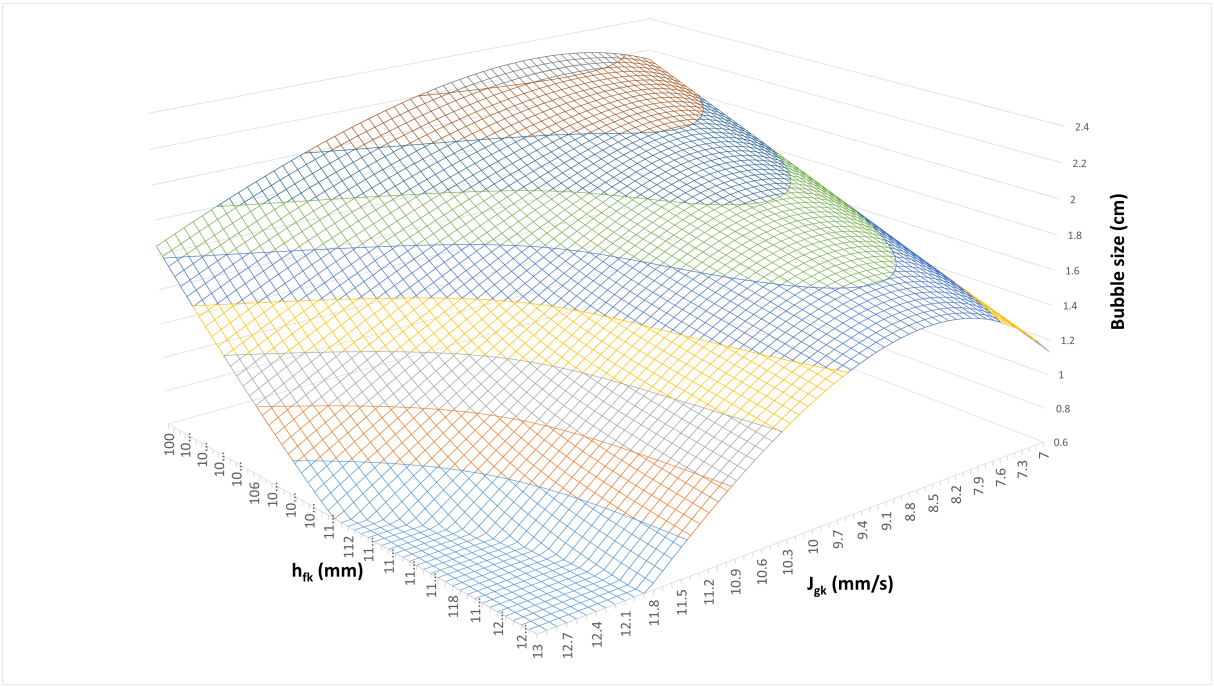

Figure 3: Top of froth bubble size, D_{BF_k}, (27) as a function of J_{g_k} and h_{f_k}

Water recovery has a quadratic dependence on J_{g_k}, and an inverse dependence on bubble size, which results in some interesting variations in entrainment over a range for J_{g_k} and h_{f_k} as shown in Fig. 5.

When the true flotation and entrainment components are combined, concentrate grade (as shown in Fig. 6) increases with an increase in h_{f_k} and a decrease in J_{g_k} as expected. Recovery, as shown in Fig. 7, however shows a strong dependence on air recovery, implying that the same concentrate grade can be obtained at multiple recoveries, confirming that h_{f_k} and J_{g_k} cannot be considered independently when optimising grade and recovery in a flotation cell.

The maximum recovery shown in Fig. 7 is 45.8% when the cell is operated at $J_{g_k} = 9.7mm/s$ and $h_{f_k} = 100mm$. Fig. 6 shows a grade of 30.1% at this operating point, which can also be achieved at various other operating points. If the flotation cell was for example operated at $J_{g_k} = 7.4mm/s$ and $h_{f_k} = 108mm$, the same grade of 30.1% would have been achieved, but at a recovery of only 37.4%. In a flotation circuit,

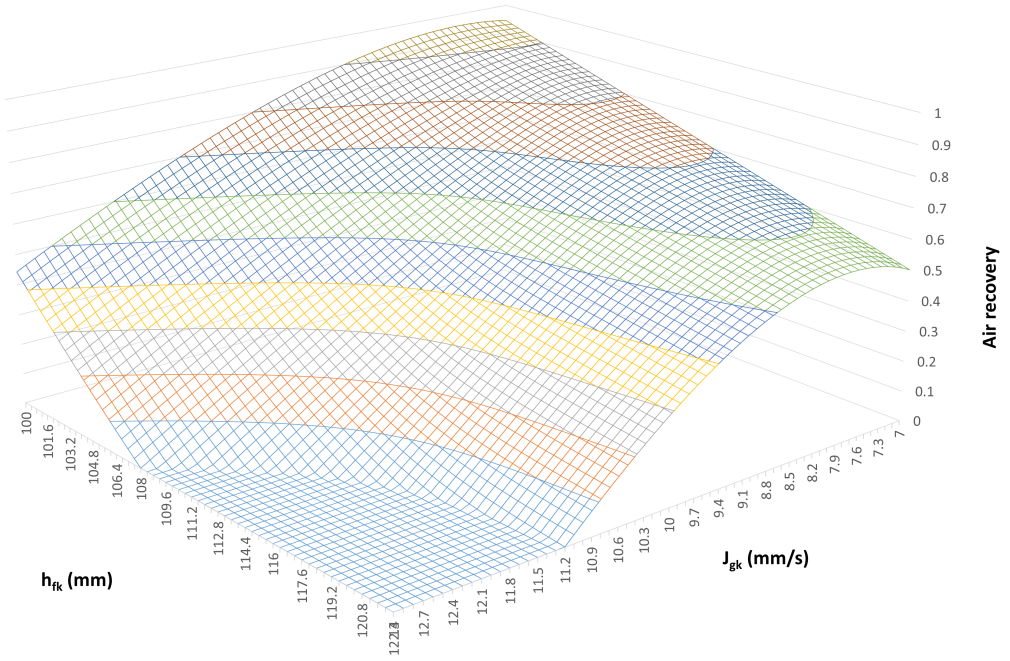

Figure 4: Air recovery, α_k, (28) as a function of J_{g_k} and h_{f_k}

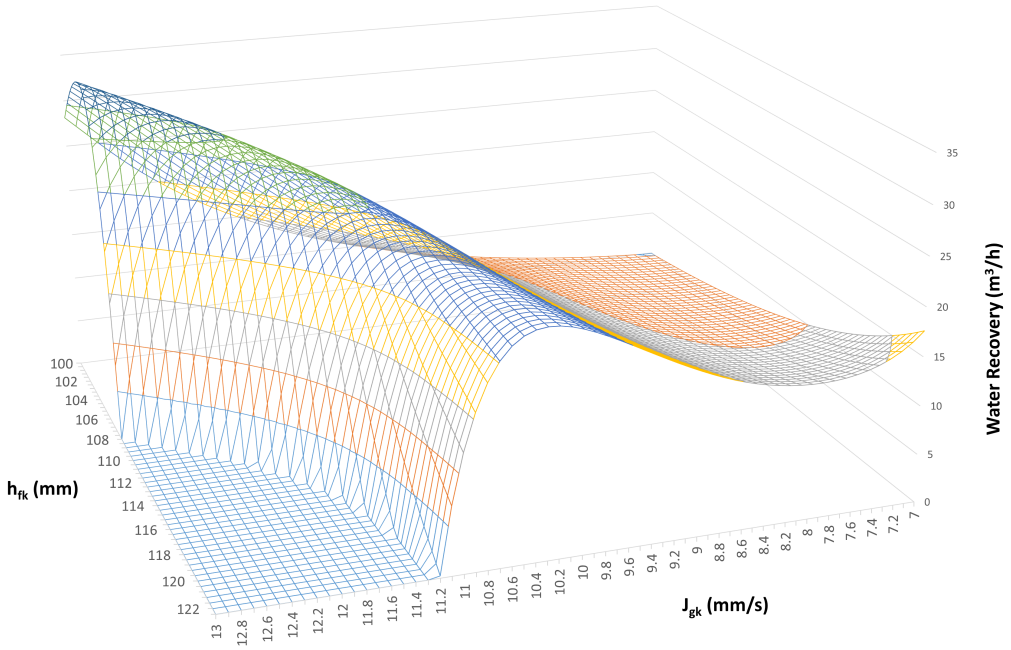

Figure 5: Water Recovery, Q_{C_k}, (7) as a function of J_{g_k} and h_{f_k}

there is still an opportunity to recover more of the desired minerals in downstream cells, where upstream cells are not operated at their recovery peaks. The masses of desired minerals available in downstream cells, are also a function of the recoveries in upstream cells, as indicated by the mass balance (3). This quantitative example provides an indication of the potential benefit that model-based control could have on improving recoveries in flotation processes.

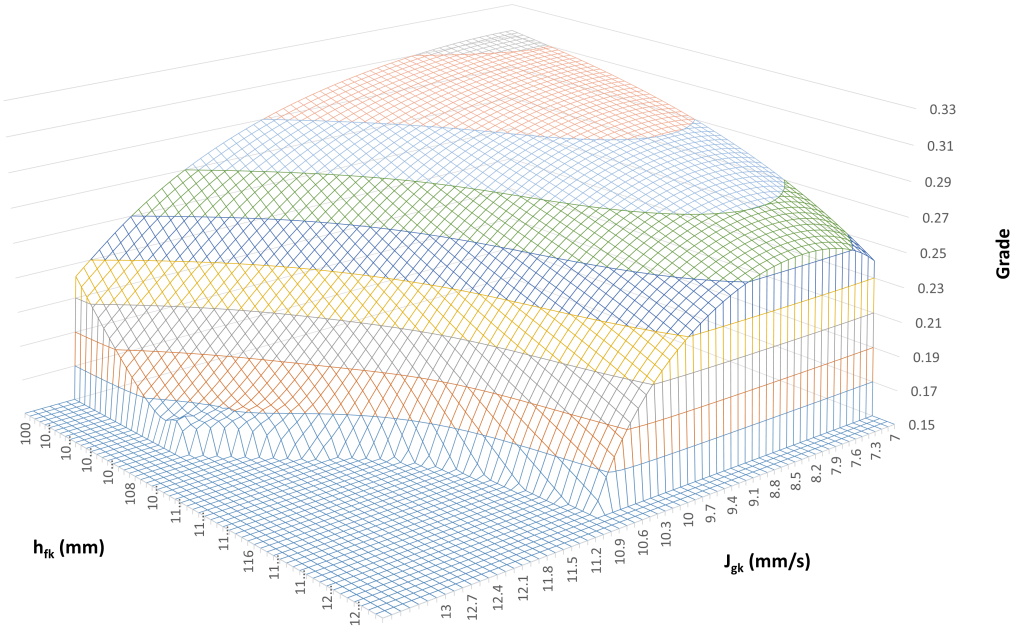

Figure 6: Concentrate Grade, $Grade_{C_k}$, (24) as a function of J_{g_k} and h_{f_k}

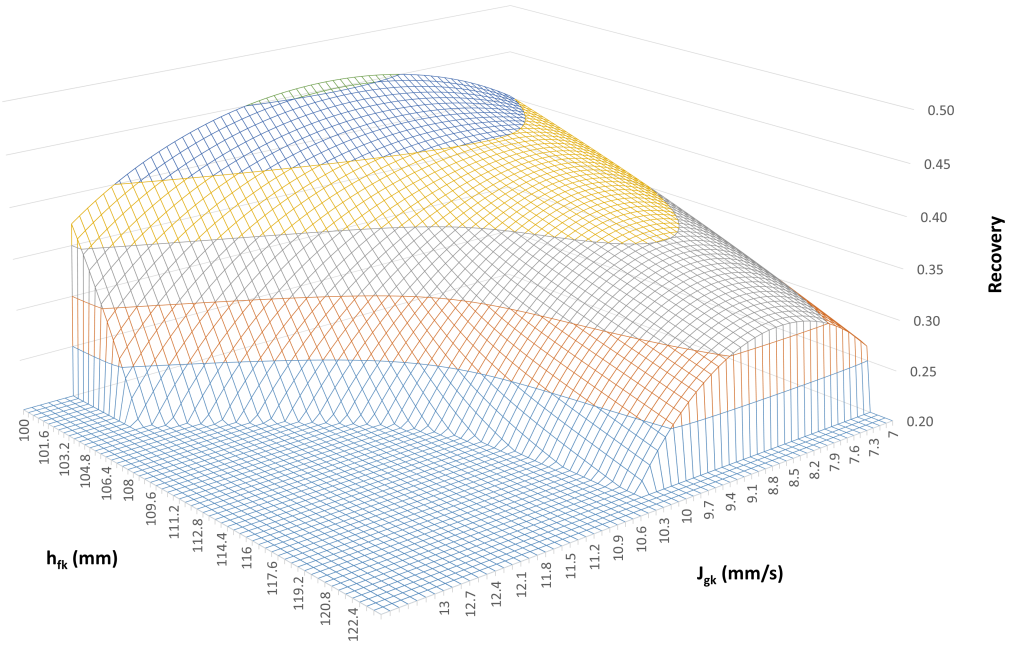

Figure 7: Concentrate Recovery, Rec_{C_k}, (25) as a function of J_{g_k} and h_{f_k}

4. Dynamic Model Analysis

The dynamic model analysis has two objectives:

- To determine if the model parameters (that would normally be calculated from a manual sampling campaign) can be estimated continuously from online measurements, defined as measured model outputs. The observability analyses shown in Sections 4.1 - 4.3 evaluate different combinations of model states and measurements to show which measurements are required to estimate specific sets of parameters. Should an observability analysis return a negative result, the interpretation is that all model states and parameters cannot be estimated using the defined model equations and measurements. An alternative model definition with additional measurements (which may include derivatives of existing measurements), a reduced parameter set or alternative model equations would be necessary to estimate all models states and parameters.
- To determine if the model states can be controlled to desired setpoints using the defined model inputs. This is evaluated using a controllability analysis as described in Section 4.4. Similar to the observability analysis, if all the states are not controllable, it means that the states cannot be driven to a specific operating condition given the available inputs. Note that the controllability analysis does not provide any conclusion on the operating ranges of the model inputs relative to the desired model states.

The dynamic flotation model can be analysed by dividing it into three parts: the parameter estimation for froth bubble size and α_k, the volume balance and the mass balance. The flotation model can be represented in state-space format, with $\mathbf{x}$ the states, $\mathbf{u}$ the manipulated variables and $\mathbf{y}$ the measured variables:

$$\begin{aligned} \frac{d\mathbf{x}}{dt} &= \mathbf{f}(t, \mathbf{x}, \mathbf{u}) \\ \mathbf{y} &= \mathbf{h}(t, \mathbf{x}, \mathbf{u}) \end{aligned} \tag{30}$$

The non-linear system can be linearised at a steady-state operating point, ($\mathbf{x}_0$,$\mathbf{u}_0$), with the deviation variables defined as $\delta\mathbf{x} = \mathbf{x} - \mathbf{x}_0$, $\delta\mathbf{u} = \mathbf{u} - \mathbf{u}_0$ and $\delta\mathbf{y} = \mathbf{y} - \mathbf{y}_0$.

$$\begin{aligned} \frac{d}{dt}\delta\mathbf{x} =& \mathbf{A}\delta\mathbf{x} + \mathbf{B}\delta\mathbf{u} \\ \delta\mathbf{y} =& \mathbf{C}\delta\mathbf{x} + \mathbf{D}\delta\mathbf{u} \end{aligned} \tag{31}$$

The system matrices, $\mathbf{A}$, $\mathbf{B}$, $\mathbf{C}$ and $\mathbf{D}$ can be calculated as:

$$\begin{aligned} \mathbf{A} &= \left.\frac{\partial \mathbf{f}(t,\mathbf{x},\mathbf{u})}{\partial \mathbf{x}}\right|_{\mathbf{x}_0,\mathbf{u}_0} & \mathbf{B} &= \left.\frac{\partial \mathbf{f}(t,\mathbf{x},\mathbf{u})}{\partial \mathbf{u}}\right|_{\mathbf{x}_0,\mathbf{u}_0} \\ \mathbf{C} &= \left.\frac{\partial \mathbf{h}(t,\mathbf{x},\mathbf{u})}{\partial \mathbf{x}}\right|_{\mathbf{x}_0,\mathbf{u}_0} & \mathbf{D} &= \left.\frac{\partial \mathbf{h}(t,\mathbf{x},\mathbf{u})}{\partial \mathbf{u}}\right|_{\mathbf{x}_0,\mathbf{u}_0} \end{aligned} \tag{32}$$

Skogestad and Postlehwaite (2005) describe how state observability and state controllability can be analysed for linear systems by determining the rank of an observability ($\mathcal{O}$) and controllability ($\mathcal{C}$) matrix respectively. If the linearised system is observable or controllable, it implies that the non-linear system is also observable or controllable (Hermann and Krener, 1977; le Roux et al., 2017). All the states, $\mathbf{x}$, are said to be observable or controllable from the input vector, $\mathbf{u}$, and output vector, $\mathbf{y}$, if $\mathcal{O}$ or $\mathcal{C}$ has full rank, n, where n is the dimension of the state vector $\mathbf{x}$. This technique can also be used to determine if model parameters can be estimated from $\mathbf{u}$ and $\mathbf{y}$, by augmenting the state vector $\mathbf{x}$, with the model parameters as states without any dynamics (Simon, 2006). The state observability matrix is shown in (33) and the state controllability matrix in (34).

$$\mathcal{O} = \begin{bmatrix} \mathbf{C} \\ \mathbf{CA} \\ \vdots \\ \mathbf{CA}^{n-1} \end{bmatrix} \tag{33}$$

$$\mathcal{C} = \begin{bmatrix} \mathbf{B} & \mathbf{AB} & \mathbf{A}^2\mathbf{B} & \dots & \mathbf{A}^{n-1}\mathbf{B} \end{bmatrix} \tag{34}$$

4.1. Parameter estimation of froth bubble size and air recovery

The state equations for D_{BF_k}, D_{BF_k} and α_k, are shown in Table 4. Estimation of $K_{\alpha_{BF}}$, $K_{\alpha_{J_g}}$, $K_{BS_{J_g}}$ and K_{BS_λ} are trivial as these parameters can be determined from multiple data-points using linear regression techniques. To include estimation of these empirical parameters into the overall flotation model analysis, $K_{\alpha_{BF}}$, $K_{\alpha_{J_g}}$, $K_{BS_{J_g}}$ and K_{BS_λ} are defined as state variables $\mathbf{x}_{p1}$, with zero dynamics. The augmented state vector $\mathbf{x}_{aug1}$, include $\mathbf{x}_1$, the original state vector, and $\mathbf{x}_{p1}$. Analogous to multiple measurements being required to calculate the parameters using regression techniques, derivatives of manipulated variables $\mathbf{u}$, and outputs $\mathbf{y}$, are required to satisfy observability requirements, if a single flotation cell is considered. An alternative approach is to use measurements from multiple cells, which removes the requirement for higher order derivatives. Measurements from two flotation cells will be included for this analysis.

The state ($\mathbf{x}_{ck}$), output ($\mathbf{y}_{ck}$) and input ($\mathbf{u}_{ck}$) vectors for a single flotation cell, k, are given in (35), followed by the state ($\mathbf{x}_1$) and output ($\mathbf{y}_1$) and input ($\mathbf{u}_1$) vectors for two cells. The observability analysis is performed using the augmented state vector $\mathbf{x}_{aug1}$, and output vector $\mathbf{y}_1$. A full rank of 8 is achieved, indicating that all the states in $\mathbf{x}_{aug1}$ can be estimated from the measurements in $\mathbf{y}_1$.

$$
\begin{aligned}
\mathbf{y}_{ck} &= [D_{BF_k}, \alpha_k]^T \\
\mathbf{x}_{ck} &= [D_{BF_k}, \alpha_k]^T \\
\mathbf{u}_{ck} &= [J_{g_k}, h_{f_k}]^T \\
\\
\mathbf{y}_1 &= [\mathbf{y}_{c1}^T, \mathbf{y}_{c2}^T]^T \\
\mathbf{x}_1 &= [\mathbf{x}_{c1}^T, \mathbf{x}_{c2}^T]^T \\
\mathbf{u}_1 &= [\mathbf{u}_{c1}^T, \mathbf{u}_{c2}^T]^T \\
\\
\mathbf{x}_{p1} &= [K_{BS_{J_g}}, K_{BS_\lambda}, K_{\alpha_{BF}}, K_{\alpha_{J_g}}]^T \\
\mathbf{x}_{aug1} &= [\mathbf{x}_1^T, \mathbf{x}_{p1}^T]^T
\end{aligned}
\tag{35}
$$

4.2. Parameter estimation including the volume balance

The outflow rate from the concentrate hopper (Q_H) is often manipulated to achieve a desired mass-pull (the flow rate of solids reporting to the concentrate), and the concentrate hopper level (L_H) is typically measured. The measurement of L_H allows C_{PB} (a state with zero dynamics) to be estimated, which also allows the concentrate flow rates from all flotation cells to be estimated using (2), and (7) to (9). The required states and measurements to estimate C_{PB} are given in (36), for the circuit with a hopper and two flotation cells defined in (35). The resulting observability matrix has a full rank of 10, confirming that C_{PB} can be estimated from (36).

$$
\begin{aligned}
\mathbf{y}_2 &= [\mathbf{y}_1^T, L_H]^T \\
\mathbf{x}_2 &= [\mathbf{x}_1^T, L_H]^T \\
\mathbf{u}_2 &= [\mathbf{u}_1^T, Q_H]^T \\
\mathbf{x}_{p2} &= [\mathbf{x}_{p1}^T, C_{PB}]^T \\
\mathbf{x}_{aug2} &= [\mathbf{x}_2^T, \mathbf{x}_{p2}^T]^T
\end{aligned}
\tag{36}
$$

Estimation of the tailings flow rates (Q_{T_k}) for each flotation cell using (1), requires that the flotation cell levels (L_k) also be measured. The states and measurements required together with those detailed in (36) to estimate the tailings flow rates (with zero dynamics) from three cells, are given by (37). The states and measurements for each cell are shown in ($\mathbf{x}_{ck}$) and ($\mathbf{y}_{ck}$). The system analysis was expanded to include 3 flotation cells with concentrate flow rates into the same concentrate hopper. The resulting observability matrix has a full rank of 18.

$$
\begin{aligned}
\mathbf{y}_{ck} &= [D_{BF_k}, \alpha_k, L_k]^T \\
\mathbf{x}_{ck} &= [D_{BF_k}, \alpha_k, L_k]^T \\
\mathbf{u}_{ck} &= [J_{g_k}, h_{f_k}]^T \\
\\
\mathbf{y}_3 &= [\mathbf{y}_{c1}^T, \mathbf{y}_{c2}^T, \mathbf{y}_{c3}^T, L_H]^T \\
\mathbf{x}_3 &= [\mathbf{x}_{c1}^T, \mathbf{x}_{c2}^T, \mathbf{x}_{c3}^T, L_H]^T \\
\mathbf{u}_3 &= [\mathbf{u}_{c1}^T, \mathbf{u}_{c2}^T, \mathbf{u}_{c3}^T, Q_H]^T \\
\\
\mathbf{x}_{p3} &= [\mathbf{x}_{p2}^T, Q_{T_1}, Q_{T_2}, Q_{T_3}]^T \\
\mathbf{x}_{aug3} &= [\mathbf{x}_3^T, \mathbf{x}_{p3}^T]^T
\end{aligned}
\tag{37}
$$

4.3. Parameter estimation including the mass balance

For the model analysis, 2 mineral species are included (chalcopyrite ($i = 0$) and gangue minerals ($i = 1$)) (Hadler et al., 2010), which can be generalised to be the desired (floatable) and undesired (mostly entrained)

mineral species. A single class ($j = 0$) is defined for each of these species. This approximation hence does not subdivide each class into multiple size distributions (d_{pmin} and d_{pmax}) or floatability constants ($K^{i,j}$). For each flotation cell, (3) needs to be included in the model for $i = 0$ (desired mineral) and $i = 1$ (gangue mineral). Concentrate mass flow rates, $\dot{M}_{C_k}^{i,j}$, are modelled by including the true flotation and entrainment models, as shown in (22). The two mineral species are also included in the hopper model using (5), for $i = 0$ (desired mineral) and $i = 1$ (gangue mineral).

The model analysis including the mass balance equations are performed for 3 flotation cells feeding into a concentrate hopper. The 10 measurements in $\mathbf{y}_3$ (37) are required, as well as the concentrate hopper outflow grade (G_H) and total mass flow rate ($\dot{M}_H^{Tot}$) (inferred from a density measurement). For this model structure (two species and one class per species), the total mass flow rate is given in (38) and the hopper outflow grade in (39).

$$\dot{M}_H^{Tot} = \sum_{i=0}^{1}\sum_{j=0}^{0} \dot{M}_H^{i,j} \tag{38}$$

$$G_H = \frac{M_H^{0,0}}{M_H^{0,0} + M_H^{1,0}} \tag{39}$$

The state vector $\mathbf{x}_4$, is made up of the state vector $\mathbf{x}_3$ in (37) and 8 additional states that are comprised of the masses of each of the two species in each flotation cell ($M_k^{i,j}$) and in the concentrate hopper ($M_H^{i,j}$). The states and measurements applicable to the flotation bank - not a specific cell - are lumped together under $\mathbf{x}_C$ and $\mathbf{y}_C$ respectively in (40). As the tailings flow rates between flotation cells (Q_{T_k}) are typically manipulated to control the levels in flotation cells (L_k), Q_{T_k} is included in the input vector ($\mathbf{u}_{ck}$) in this and the controllability analysis in Section 4.4, rather than in the parameter vector $\mathbf{x}_{p4}$ as was done in (37). The dimensions of $\mathbf{x}_{aug4}$ is 23 x 1, including the 18 states in $\mathbf{x}_4$ and the 5 parameters in $\mathbf{x}_{p4}$. The observability matrix of this system has full column rank of 23, implying that the masses of the desired and gangue minerals in all flotation cells as well as the concentrate hopper can be estimated from the online measurements in $\mathbf{y}_4$ (40).

$$\begin{aligned}
\mathbf{y}_{ck} &= [D_{BF_k}, \alpha_k, L_k]^T \\
\mathbf{x}_{ck} &= [D_{BF_k}, \alpha_k, L_k, M_k^{0,0}, M_k^{1,0}]^T \\
\mathbf{u}_{ck} &= [J_{g_k}, h_{f_k}, Q_{T_k}]^T \\
\mathbf{y}_C &= [L_H, G_H, \dot{M}_H^{Tot}]^T \\
\mathbf{x}_C &= [L_H, M_H^{0,0}, M_H^{1,0}]^T \\
\mathbf{y}_4 &= [\mathbf{y}_{c1}^T, \mathbf{y}_{c2}^T, \mathbf{y}_{c3}^T, \mathbf{y}_C^T]^T \\
\mathbf{x}_4 &= [\mathbf{x}_{c1}^T, \mathbf{x}_{c2}^T, \mathbf{x}_{c3}^T, \mathbf{x}_C^T]^T \\
\mathbf{u}_4 &= [\mathbf{u}_{c1}^T, \mathbf{u}_{c2}^T, \mathbf{u}_{c3}^T, Q_H]^T \\
\mathbf{x}_{p4} &= [K_{BS_{Jg}}, K_{BS_\lambda}, K_{\alpha_{BF}}, K_{\alpha_{Jg}}, C_{PB}]^T \\
\mathbf{x}_{aug4} &= [\mathbf{x}_4^T, \mathbf{x}_{p4}^T]^T
\end{aligned} \tag{40}$$

It may theoretically be possible to determine the flotation rate constants of the two mineral species, $K^{i,j}$, defined in (12) from online measurements, by adding additional derivatives of concentrate grade (G_H) and mass flow rate ($\dot{M}^{Tot}$). Given typical measurement noise levels on industrial plants, and considering that some process variables (for example mass flow rates) rely on a combination of measurements (density and volumetric flow rate), such an approach is unlikely to be reliable in an industrial environment.

An alternative, more robust approach, is to only perform the estimation of $K^{i,j}$ when the process is at steady-state, or to use the average of multiple measurements (approximating steady-state operation). At steady-state, mass derivative terms in (3) ($\frac{d}{dt}M_k^{i,j}$) and (5) ($\frac{d}{dt}M_H^{i,j}$) would be zero, allowing the mass flow

rates in the flotation cells (3) and concentrate hopper (5) to be calculated from inferred mass flow rates of the feed, $\dot{M}_{F_1}^{i,j}$, and similarly for the concentrate, $\dot{M}_H^{i,j}$. Noting that at steady-state, the tailings mass flow rate from the last flotation cell, $\dot{M}_{T_3}^{i,j}$, would be the difference between the feed mass flow rate to the first flotation cell, $\dot{M}_{F_1}^{i,j}$, and the concentrate hopper mass flow rate, $\dot{M}_H^{i,j}$, as described in (41), the steady-state mass balance can be solved.

$$\dot{M}_{T_3}^{i,j} = \dot{M}_{F_1}^{i,j} - \dot{M}_H^{i,j} \tag{41}$$

For the steady-state observability analysis, one can include $\dot{M}_{T_3}^{i,j}$ for the desired and gangue minerals as additional measurements to $\mathbf{y}_4$, defined in (40). The two reaction rate constants for the desired and gangue minerals, $K^{i,j}$, are added to $\mathbf{x}_{p4}$, the parameter vector, as shown in (42). With the steady-state approximation, a full rank of 25 is achieved, indicating that the flotation rate constants of the desired and gangue minerals, $K^{i,j}$, can be estimated from online measurements when a steady-state approximation is used.

$$\begin{aligned}
\mathbf{y}_5 &= [\mathbf{y}_4^T, \dot{M}_{T_3}^{0,0}, \dot{M}_{T_3}^{1,0}]^T \\
\mathbf{x}_5 &= [\mathbf{x}_4] \\
\mathbf{x}_{p5} &= [\mathbf{x}_{p4}^T, K^{0,0}, K^{1,0}]^T \\
\mathbf{x}_{aug5} &= [\mathbf{x}_5^T, \mathbf{x}_{p5}^T]^T
\end{aligned} \tag{42}$$

4.4. Controllability

The state controllability of the linear system is analysed to determine if the states, $\mathbf{x}_4$ described in (40) (and repeated in (43)) can be controlled using the manipulated variables, $\mathbf{u}_6$ in (43). The objective is to determine if the grade of the flotation bank (G_H - measured at the outflow from the concentrate hopper) can be controlled, while also controlling the air recoveries of all cells at their maximums, which is equivalent to operating at the maximum recovery point for each cell, for a given h_{f_k} (Hadler et al., 2010). Full rank of 18 is achieved for the state controllability matrix, $\mathcal{C}$, defined in (34), indicating that all 18 states in $\mathbf{x}_6$ can be controlled using the aeration rates (J_{g_k}), froth depths (h_{f_k}) and tailings flow rates (Q_{T_k}) in all the flotation cells in combination with the concentrate hopper outflow rate (Q_H).

$$\begin{aligned}
\mathbf{x}_{ck} &= [D_{BF_k}, \alpha_k, L_k, M_k^{0,0}, M_k^{1,0}]^T \\
\mathbf{u}_{ck} &= [J_{g_k}, h_{f_k}, , Q_{T_k}]^T \\
\mathbf{x}_C &= [L_H, M_H^{0,0}, M_H^{1,0}]^T \\
\mathbf{y}_6 &= [\mathbf{y}_{c0}^T, \mathbf{y}_{c1}^T, \mathbf{y}_{c2}^T, \mathbf{y}_C^T]^T \\
\mathbf{x}_6 &= [\mathbf{x}_{c0}^T, \mathbf{x}_{c1}^T, \mathbf{x}_{c2}^T, \mathbf{x}_C^T]^T \\
\mathbf{u}_6 &= [\mathbf{u}_{c0}^T, \mathbf{u}_{c1}^T, \mathbf{u}_{c2}^T, Q_H]^T
\end{aligned} \tag{43}$$

5. Discussion

The ability to estimate model parameters for α_k and D_{BF_k} from online measurements, provide valuable information on how close to the maximum air recovery point each cell is operating and in what direction the manipulated variables, J_{g_k} and h_{f_k}, should be moved to optimise operation. Combining the estimated maximum air-recovery point with a model for D_{BF_k} (which has a strong influence on entrainment, and hence grade), open up opportunities to optimise both grade and recovery, and also to include additional manipulated variables such as frother addition into an optimisation strategy.

The volume balance and associated observability analysis (allowing C_{PB} to be estimated), allow the concentrate volume produced by each cell to be calculated. This provides a good indication of the relative contribution of each cell to the total entrained mass - even without considering the mass balance. A reduction

in the entrained concentrate volume from a cell results in an increase in grade. The quadratic relationship between water recovery and D_{BF_k}, shown in Fig. 5, highlights the importance of including an online measure of froth bubble size as part of an optimisation strategy.

The mass balance provides invaluable information in distinguishing between true flotation and entrainment in the concentrate stream from each cell. This is the key to optimise reagent addition, as the reason for excessive gangue minerals in the concentrate stream can be identified as either insufficient suppression or excessive entrainment. An estimate of the relative contribution from each cell to the overall concentrate stream, allows for optimisation across multiple cells, to achieve optimal operation. The ability to estimate the flotation rate constants of the desired and gangue minerals ($K^{0,0}$ and $K^{1,0}$) from online measurements (even if limited to steady-state operation) opens a range of opportunities to optimise reagent additions (depressants and collectors) and to react to short-term variations in ore characteristics that occur between sampling campaigns. While mass flow rate measurements on the concentrate streams from each flotation cell is often impractical to install, there is scope to include other image qualities from froth imaging devices to quantify the relative contributions from multiple cells.

While the observability analysis confirm that valuable process parameters can be estimated from online measurements, the controllability analysis confirms that a model-based automatic control strategy can be used to optimise a flotation process. Control variables that are commonly available on industrial plants (J_{g_k}, h_{f_k}, Q_{T_k} and Q_H) are sufficient to control the concentrate grade and air recovery α_k, while regulating the concentrate hopper level L_H, and flotation cell levels L_k. Being able to control α_k in each cell implies that each cell can be controlled at its peak air recovery (α_k) at all times, using a model-based controller instead of relying on an iterative stepping algorithm.

The main aim of a flotation plant is to produce a product of a desired grade. Being able to control grade in combination with operating at the maximum air recovery (α_k) (which is associated with maximum recovery (Hadler et al., 2012)) is an important step towards optimising flotation operation.

6. Conclusion

A flotation model was described that can model the effect of variations in aeration rate (J_{g_k}) and froth depth (h_{f_k}) on multiple mineral species, and how the contribution from each species influences the concentrate hopper and tailings grade and recovery of a flotation bank. An observability analysis showed that floatability constants of desired and gangue minerals can be estimated using online measurements. A controllability analysis confirmed that the modelled states can be controlled using aeration rate (J_{g_k}), froth depth (h_{f_k}), tailings flow rates (Q_{T_k}) and concentrate hopper flow rate (Q_H), and that the process can consequently be controlled at an optimum air recovery point while maintaining a desired grade.

The combination of fundamental dynamic mass and volume balances, steady-state flotation froth models and empirical relations on air recovery and froth bubble size, allows key characteristics of flotation processes to be estimated from online measurements. This opens up opportunities to control the flotation process more efficiently, and to include reagent addition in the set of manipulated variables based on real-time estimates of true flotation and entrainment of desired and gangue minerals. Further refinements to the model developed in this work can be made to include frother, depressants and activators in the set of control variables, and there is potentially an opportunity to use froth image data from multiple cells to enhance observability of model states related to relative concentrate mass flow rates under time-varying operation.

7. Acknowledgement

Thanks to Kathryn Hadler and Jan Cilliers from Imperial College London for sharing information, and making the industrial data used in this study available.

This work is based on research supported in part by the National Research Foundation of South Africa (Grant number 111741).

Aldrich, C., Marais, C., Shean, B.J., Cilliers, J.J., 2010. Online monitoring and control of froth flotation systems with machine vision: A review. International Journal of Mineral Processing 96, 1–13.

Ata, S., 2008. Coalescence of bubbles covered by particles. Langmuir 24, 6085–6091.
Barbian, N., Ventura-Medina, E., Cilliers, J.J., 2003. Dynamic froth stability in froth flotation. Minerals Engineering 16, 1111–1116.
Bascur, O.A., 2005. Example of a Dynamic Flotation Framework, in: Centenary of Flotation Symposium, Brisbane. pp. 85–91.
Bascur, O.A., Herbst, J.A., 1982. Dynamic Modelling of a Flotation Cell with a view towards Automatic Control, in: XIV International Mineral Processing Conference, CIM, Toronto, Canada, pp. III–11.1–III–11.22.
Gallegos-Acevedo, P.M., Espinoza-Cuadra, J., Perez-Garibay, R., Pecina-Trevino, E.T., 2010. Bubbles Coalescense: Hydrofobic Particles Effect. Journal of Mining Science 46, 333–337.
Geldenhuys, S., McFadzean, B., 2019. The effect of pulp bubble size on the dynamic froth stability measurement. Minerals Engineering 131, 164–169.
Hadler, K., Cilliers, J.J., 2009. The relationship between the peak in air recovery and flotation bank performance. Minerals Engineering 22, 451–455.
Hadler, K., Greyling, M., Plint, N., Cilliers, J.J., 2012. The effect of froth depth on air recovery and flotation performance. Minerals Engineering 36-38, 248–253.
Hadler, K., Smith, C., Cilliers, J., 2010. Flotation performance improvement by air recovery optimisation on roughers and scavengers. XXV International Mineral Processing Congress 2010, IMPC 2010 3, 1917–1924.
Hermann, R., Krener, A.J., 1977. Nonlinear Controllability and Observability. IEEE Transactions on Automatic Control 22, 728–740.
Jämsä-Jounela, S.L., Dietrich, M., Halmevaara, K., Tiili, O., 2003. Control of pulp levels in flotation cells. Control Engineering Practice 11, 73–81.
le Roux, J., Steinboeck, A., Kugi, A., Craig, I., 2017. An ekf observer to estimate semi-autogenous grinding mill hold-ups. Journal of Process Control 51, 27 – 41.
Morar, S., Hatfield, D., Barbian, N., Bradshaw, D., Cilliers, J., Triffett, B., 2006. A comparison of flotation froth stability measurements and their use in the prediction of concentrate grade. IMPC 2006 - Proceedings of 23rd International Mineral Processing Congress .
Morar, S.H., Bradshaw, D.J., Harris, M.C., 2012. The use of the froth surface lamellae burst rate as a flotation froth stability measurement. Minerals Engineering 36-38, 152–159.
Neethling, S.J., Brito-Parada, P.R., 2018. Predicting flotation behaviour The interaction between froth stability and performance. Minerals Engineering 120, 60–65.
Neethling, S.J., Cilliers, J.J., 2003. Modelling flotation froths. International Journal of Mineral Processing 72, 267–287.
Neethling, S.J., Cilliers, J.J., 2009. The entrainment factor in froth flotation: Model for particle size and other operating parameter effects. International Journal of Mineral Processing 93, 141–148.
Oosthuizen, D.J., Craig, I.K., 2018. On the current state of flotation modelling for process control. IFAC-PapersOnLine 51, 105–110.
Polat, M., Chander, S., 2000. First-order flotation kinetics models and methods for estimation of the true distribution of flotation rate constants. International Journal of Mineral Processing 58, 145–166.
Runge, K., Franzidis, J.P., 2003. Structuring a flotation model for robust prediction of flotation circuit performance, in: XXII International Mineral Processing Congress, pp. 973–984.
Saffy, M., Mashakane, T., Hopstadius, P., 2019. Control and optimisation of a gold milling and flotation circuit. World Gold Conference, Perth, Australia .
Schubert, J., Henning, R., Hulbert, D., Craig, I., 1995. Flotation control - a multivariable stabilizer, in: XIX International Mineral Processing Conference, San Francisco, pp. 237–244.
Shean, B., Hadler, K., Neethling, S., Cilliers, J.J., 2018. A dynamic model for level prediction in aerated tanks. Minerals Engineering 125, 140–149.
Simon, D., 2006. Optimal State Estimation: Kalman, H Infinity, and Nonlinear Approaches. 1st ed., Wiley-Interscience.
Skogestad, S., Postlehwaite, I., 2005. Multivariable Feedback Control. Second edition ed., Wiley, Chichester.
Tang, J., Tan, B.S., 1989. The Effect of Silica Oxide Particles upon Stabilization of Foam. Journal of Colloid and Interface Science 131, 498–502.
Wang, L., Peng, Y., Runge, K., 2016. Entrainment in froth flotation: The degree of entrainment and its contributing factors. Powder Technology 288, 202–211.
Wills, B.A., Napier-Munn, T., 2006. Mineral Processing Technology: An Introduction to the Practical Aspects of Ore Treatment and Mineral Recovery.
Zheng, X., Franzidis, J.P., Johnson, N.W., 2006. An evaluation of different models of water recovery in flotation. Minerals Engineering 19, 871–882.

Appendix A. Linearised System Matrices

The linearised system matrices $\mathbf{A}$, $\mathbf{B}$ and $\mathbf{C}$ in (31) as described in Section 4 are shown in Appendix A.1 - Appendix A.3. For brevity, terms related to the mass balance described in Section 2.2 are not shown due to the complexity of derivatives of the entrainment equations (19) - (21). Variables in the augmented state vector $\mathbf{x}_{aug5}$ and output vector $\mathbf{y}_5$ shown in (42), and the input vector $\mathbf{u}_6$ shown in (43) are reordered as shown in (A.1).

$$
\begin{aligned}
\mathbf{u}_7 &= [J_{g_1}, h_{f_1}, J_{g_2}, h_{f_2}, J_{g_3}, h_{f_3}, Q_H, Q_{T_1}, Q_{T_2}, Q_{T_3}]^T \\
\mathbf{x}_7 &= [D_{BF_1}, \alpha_1, D_{BF_2}, \alpha_2, D_{BF_3}, \alpha_3, L_1, L_2, L_3, L_H, M_1^{0,0}, M_1^{1,0}, M_2^{0,0}, M_2^{1,0}, M_3^{0,0}, M_3^{1,0}, M_H^{0,0}, M_H^{1,0}]^T \\
\mathbf{x}_{p7} &= [K_{BS_{J_g}}, K_{BS_\lambda}, K_{\alpha_{J_g}}, K_{\alpha_{BF}}, C_{PB}, K^{0,0}, K^{1,0}]^T \\
\mathbf{x}_{aug7} &= [\mathbf{x}_7^T, \mathbf{x}_{p7}^T]^T \\
\mathbf{y}_7 &= [D_{BF_1}, \alpha_1, D_{BF_2}, \alpha_2, D_{BF_3}, \alpha_3, L_1, L_2, L_3, L_H, \dot{M}_H^{Tot}, G_H, \dot{M}_{T_3}^{0,0}, \dot{M}_{T_3}^{1,0}]^T
\end{aligned} \tag{A.1}
$$

Appendix A.1. Process matrix $\boldsymbol{A}$

The structure of the linearised process matrix $\mathbf{A}$, is shown in (A.2). $\mathbf{0}^{r\times c}$ is a zero-matrix with dimensions $r\times c$, and ${\mathbf{A}_1}^{6\times 4}$ in (A.3), ${\mathbf{A}_2}^{4\times 6}$ in (A.4) and ${\mathbf{A}_3}^{4\times 1}$ in (A.5) are sub-matrices of $\mathbf{A}$. The elements of ${\mathbf{A}_4}^{8\times 25}$ are not shown here because of space restrictions.

$$
\mathbf{A} = \left[\begin{array}{ccc|c|c}
\multicolumn{3}{c|}{\mathbf{0}^{6\times 18}} & {\mathbf{A}_1}^{6\times 4} & \mathbf{0}^{6\times 3} \\
\hline
{\mathbf{A}_2}^{4\times 6} & \mathbf{0}^{4\times 12} & \mathbf{0}^{4\times 4} & {\mathbf{A}_3}^{4\times 3} \\
\hline
\multicolumn{4}{c|}{{\mathbf{A}_4}^{8\times 25}} \\
\hline
\multicolumn{4}{c|}{\mathbf{0}^{7\times 25}}
\end{array}\right] \tag{A.2}
$$

$$
\mathbf{A}_1 = \begin{bmatrix}
J_{g_1} & \frac{h_{f_1}}{J_{g_1}} & 0 & 0 \\
J_{g_1}K_{\alpha_{BF}} & \frac{K_{\alpha_{BF}}h_{f_1}}{J_{g_1}} & J_{g_1} & J_{g_1}K_{BS_{J_g}} + \frac{K_{BS_\lambda}h_{f_1}}{J_{g_1}} \\
J_{g_2} & \frac{h_{f_2}}{J_{g_2}} & 0 & 0 \\
J_{g_2}K_{\alpha_{BF}} & \frac{K_{\alpha_{BF}}h_{f_2}}{J_{g_2}} & J_{g_2} & J_{g_2}K_{BS_{J_g}} + \frac{K_{BS_\lambda}h_{f_2}}{J_{g_2}} \\
J_{g_3} & \frac{h_{f_3}}{J_{g_3}} & 0 & 0 \\
J_{g_3}K_{\alpha_{BF}} & \frac{K_{\alpha_{BF}}h_{f_3}}{J_{g_3}} & J_{g_3} & J_{g_3}K_{BS_{J_g}} + \frac{K_{BS_\lambda}h_{f_3}}{J_{g_3}}
\end{bmatrix} \tag{A.3}
$$

$$
\mathbf{A}_2 = \begin{bmatrix}
-\frac{SubA_1\mu}{A_1\rho g} & \frac{SubA_2\mu}{A_1\rho g} & 0 & 0 & 0 & 0 \\
0 & 0 & -\frac{SubA_4\mu}{A_2\rho g} & \frac{SubA_5\mu}{A_2\rho g} & 0 & 0 \\
0 & 0 & 0 & 0 & -\frac{SubA_7\mu}{A_3\rho g} & \frac{SubA_8\mu}{A_3\rho g} \\
\frac{SubA_1\mu}{A_H\rho g} & -\frac{SubA_2\mu}{A_H\rho g} & \frac{SubA_4\mu}{A_H\rho g} & -\frac{SubA_5\mu}{A_H\rho g} & \frac{SubA_7\mu}{A_H\rho g} & -\frac{SubA_8\mu}{A_H\rho g}
\end{bmatrix} \tag{A.4}
$$

$$
\mathbf{A}_3 = \begin{bmatrix}
\frac{SubA_3\mu}{A_1\rho g} & 0 & 0 \\
\frac{SubA_6\mu}{A_2\rho g} & 0 & 0 \\
\frac{SubA_9\mu}{A_3\rho g} & 0 & 0 \\
-\frac{\mu(SubA_3+SubA_6+SubA_9)}{A_H\rho g} & 0 & 0
\end{bmatrix} \tag{A.5}
$$

$$
SubA_1 = \frac{40.86 C_{PB} J_{g_1}^2 \alpha_1 (\alpha_1 - 1)}{D_{BF_1}^3} \tag{A.6}
$$

$$
SubA_2 = \frac{20.43 C_{PB} J_{g_1}^2 (2\alpha_1 - 1)}{D_{BF_1}^2} \tag{A.7}
$$

$$SubA_3 = \frac{20.43 J_{g_1}^2 \alpha_1 (\alpha_1 - 1)}{D_{BF_1}^2} \tag{A.8}$$

$$SubA_4 = \frac{40.86 C_{PB} J_{g_2}^2 \alpha_2 (\alpha_2 - 1)}{D_{BF_2}^3} \tag{A.9}$$

$$SubA_5 = \frac{20.43 C_{PB} J_{g_2}^2 (2\alpha_2 - 1)}{D_{BF_2}^2} \tag{A.10}$$

$$SubA_6 = \frac{20.43 J_{g_2}^2 \alpha_2 (\alpha_2 - 1)}{D_{BF_2}^2} \tag{A.11}$$

$$SubA_7 = \frac{40.86 C_{PB} J_{g_3}^2 \alpha_3 (\alpha_3 - 1)}{D_{BF_3}^3} \tag{A.12}$$

$$SubA_8 = \frac{20.43 C_{PB} J_{g_3}^2 (2\alpha_3 - 1)}{D_{BF_3}^2} \tag{A.13}$$

$$SubA_9 = \frac{20.43 J_{g_3}^2 \alpha_3 \mu (\alpha_3 - 1)}{D_{BF_3}^2} \tag{A.14}$$

Appendix A.2. Input matrix $\boldsymbol{B}$

The structure of the linearised input matrix $\mathbf{B}$, is shown in (A.15). The elements in rows 11 - 18 include derivatives of the entrainment equations (19) - (21), and are lumped into a sub-matrix $\mathbf{B}_3$ which is not shown here because of space restrictions. ${\mathbf{B}_1}^{10\times3}$ in (A.16) and ${\mathbf{B}_2}^{10\times7}$ in (A.17) are sub-matrices of $\mathbf{B}$.

$$\mathbf{B} = \left[\begin{array}{c|c} {\mathbf{B}_1}^{10\times3} & {\mathbf{B}_2}^{10\times7} \\ \hline \multicolumn{2}{c}{{\mathbf{B}_3}^{8\times10}} \\ \hline \multicolumn{2}{c}{{\mathbf{0}}^{7\times10}} \end{array}\right] \tag{A.15}$$

$$\mathbf{B}_1 = \begin{bmatrix} K_{BS_{J_g}} - \frac{K_{BS_\lambda} h_{f_1}}{J_{g_1}^2} & \frac{K_{BS_\lambda}}{J_{g_1}} & 0 \\ K_{\alpha_{BF}} \left(K_{BS_{J_g}} - \frac{K_{BS_\lambda} h_{f_1}}{J_{g_1}^2} \right) + K_{\alpha_{J_g}} & \frac{K_{BS_\lambda} K_{\alpha_{BF}}}{J_{g_1}} & 0 \\ 0 & 0 & K_{BS_{J_g}} - \frac{K_{BS_\lambda} h_{f_2}}{J_{g_2}^2} \\ 0 & 0 & K_{\alpha_{BF}} \left(K_{BS_{J_g}} - \frac{K_{BS_\lambda} h_{f_2}}{J_{g_2}^2} \right) + K_{\alpha_{J_g}} \\ 0 & 0 & 0 \\ 0 & 0 & 0 \\ -\frac{40.86 C_{PB} J_{g_1} \alpha_1 \mu (1-\alpha_1)}{A_1 D_{BF_1}^2 \rho g} & 0 & 0 \\ 0 & 0 & -\frac{40.86 C_{PB} J_{g_2} \alpha_2 \mu (1-\alpha_2)}{A_2 D_{BF_2}^2 \rho g} \\ 0 & 0 & 0 \\ \frac{40.86 C_{PB} J_{g_1} \alpha_1 \mu (1-\alpha_1)}{A_H D_{BF_1}^2 \rho g} & 0 & \frac{40.86 C_{PB} J_{g_2} \alpha_2 \mu (1-\alpha_2)}{A_H D_{BF_2}^2 \rho g} \end{bmatrix} \tag{A.16}$$

$$\mathbf{B}_2 = \begin{bmatrix} 0 & 0 & 0 & 0 & 0 & 0 & 0 \\ 0 & 0 & 0 & 0 & 0 & 0 & 0 \\ \frac{K_{BS_\lambda}}{J_{g_2}} & 0 & 0 & 0 & 0 & 0 & 0 \\ \frac{K_{BS_\lambda} K_{\alpha_{BF}}}{J_{g_2}} & 0 & 0 & 0 & 0 & 0 & 0 \\ 0 & K_{BS_{J_g}} - \frac{K_{BS_\lambda} h_{f_3}}{J_{g_3}^2} & \frac{K_{BS_\lambda}}{J_{g_3}} & 0 & 0 & 0 & 0 \\ 0 & K_{\alpha_{BF}} \left(K_{BS_{J_g}} - \frac{K_{BS_\lambda} h_{f_3}}{J_{g_3}^2} \right) + K_{\alpha_{J_g}} & \frac{K_{BS_\lambda} K_{\alpha_{BF}}}{J_{g_3}} & 0 & 0 & 0 & 0 \\ 0 & 0 & 0 & 0 & -\frac{1}{A_1} & 0 & 0 \\ 0 & 0 & 0 & 0 & \frac{1}{A_2} & -\frac{1}{A_2} & 0 \\ 0 & -\frac{40.86 C_{PB} J_{g_3} \alpha_3 \mu (1-\alpha_3)}{A_3 D_{BF_3}^2 \rho g} & 0 & 0 & 0 & \frac{1}{A_3} & -\frac{1}{A_3} \\ 0 & \frac{40.86 C_{PB} J_{g_3} \alpha_3 \mu (1-\alpha_3)}{A_H D_{BF_3}^2 \rho g} & 0 & -\frac{1}{A_H} & 0 & 0 & 0 \end{bmatrix} \tag{A.17}$$

Appendix A.3. Output matrix $\boldsymbol{C}$

The linearised output matrix $\mathbf{C}$, is a sparse matrix, with its structure shown in (A.18). $\mathbf{I}^{r \times r}$ is an identity matrix with r rows and columns, and ${\mathbf{C}_1}^{6\times4}$ in (A.19) is a sub-matrix of $\mathbf{C}$.

$$\mathbf{C} = \left[\begin{array}{c|c|c} \mathbf{I}^{9\times9} & \mathbf{0}^{9\times9} & \\ \hline \mathbf{0}^{5\times9} & {\mathbf{C}_1}^{5\times9} & \mathbf{0}^{14\times7} \end{array}\right] \tag{A.18}$$

$$\mathbf{C}_1 = \begin{bmatrix} 1 & 0 & 0 & 0 & 0 & 0 & 0 & 0 & 0 \\ -\frac{Q_H \left(M_H^{0,0} + M_H^{1,0}\right)}{A_H L_H^2} & 0 & 0 & 0 & 0 & 0 & 0 & \frac{Q_H}{A_H L_H} & \frac{Q_H}{A_H L_H} \\ 0 & 0 & 0 & 0 & 0 & 0 & 0 & -\frac{M_H^{0,0}}{\left(M_H^{0,0}+M_H^{1,0}\right)^2} + \frac{1}{M_H^{0,0}+M_H^{1,0}} & -\frac{M_H^{0,0}}{\left(M_H^{0,0}+M_H^{1,0}\right)^2} \\ 0 & 0 & 0 & 0 & 0 & 1 & 0 & 0 & 0 \\ 0 & 0 & 0 & 0 & 0 & 0 & 1 & 0 & 0 \end{bmatrix} \tag{A.19}$$